

Effects of turbulence on the mean pressure field in the separated-reattaching flow above a low-rise building

Wu, C.-H.; Akon, A.F.; Kopp, Gregory

DOI:

[10.1016/j.jweia.2017.09.013](https://doi.org/10.1016/j.jweia.2017.09.013)

License:

Creative Commons: Attribution-NonCommercial-NoDerivs (CC BY-NC-ND)

Document Version

Peer reviewed version

Citation for published version (Harvard):

Wu, C-H, Akon, AF & Kopp, G 2017, 'Effects of turbulence on the mean pressure field in the separated-reattaching flow above a low-rise building', *Journal of Wind Engineering and Industrial Aerodynamics*, vol. 171, pp. 79-92. <https://doi.org/10.1016/j.jweia.2017.09.013>

[Link to publication on Research at Birmingham portal](#)

General rights

Unless a licence is specified above, all rights (including copyright and moral rights) in this document are retained by the authors and/or the copyright holders. The express permission of the copyright holder must be obtained for any use of this material other than for purposes permitted by law.

- Users may freely distribute the URL that is used to identify this publication.
- Users may download and/or print one copy of the publication from the University of Birmingham research portal for the purpose of private study or non-commercial research.
- User may use extracts from the document in line with the concept of 'fair dealing' under the Copyright, Designs and Patents Act 1988 (?)
- Users may not further distribute the material nor use it for the purposes of commercial gain.

Where a licence is displayed above, please note the terms and conditions of the licence govern your use of this document.

When citing, please reference the published version.

Take down policy

While the University of Birmingham exercises care and attention in making items available there are rare occasions when an item has been uploaded in error or has been deemed to be commercially or otherwise sensitive.

If you believe that this is the case for this document, please contact UBIRA@lists.bham.ac.uk providing details and we will remove access to the work immediately and investigate.

1 Effects of turbulence on the mean pressure field in the separated-reattaching flow above a
2 low-rise building

3
4 Chieh-Hsun Wu, Abul Fahad Akon, Gregory A. Kopp
5 Boundary Layer Wind Tunnel Laboratory, Faculty of Engineering,
6 University of Western Ontario, London, ON, Canada N6A 5B9
7

8 Correspondence: Gregory A. Kopp

9 Boundary Layer Wind Tunnel Laboratory, Faculty of Engineering, University of Western
10 Ontario, London, ON, Canada N6A 5B9

11 Email: gakkopp@uwo.ca; Tel: 519-661-2111 ext. 87572; Fax: 519-661-3339
12

13 **Abstract**

14 The effects of upstream turbulence in the atmospheric boundary layer flow on the mean
15 surface pressure distribution within the separated flow above a typical low-rise building roof are
16 investigated experimentally. Time-averaged Navier-Stokes equations are used to evaluate the
17 pressure gradients from planar particle image velocimetry data. The pressure fields are
18 reconstructed by integrating the pressure gradients using an analytic interpolation approach.
19 This reconstruction approach is validated by successfully matching the reconstructed pressure to
20 Bernoulli's equation along a streamline far from the body and with pressure measurements on
21 the surface of the body. Through this process, the mean pressure field can be directly explained
22 from the mean velocity and turbulence fields near the roof. For high turbulence intensity levels,
23 the maximum suction coefficient on the roof surface was found to be increased. Such increased
24 magnitudes are directly related to the reduced size of mean separation bubble in higher
25 turbulence, more rapid variation of the velocity magnitude near the leading edge, and enhanced
26 variation of the turbulence stresses. On the other hand, a higher rate of surface pressure recovery
27 is found in the leeward portion of the separation bubble, which is mainly due to the more rapid
28 variation of the turbulence stresses.
29

30 **Keywords**

31 Pressure integration methods; turbulent shear flows; separating-reattaching flows; building

32 aerodynamics.

33

34 **Nomenclature**

| | | |
|----|---------------------|---|
| 35 | C_p | Pressure coefficient. |
| 36 | C_{p_e} | Estimated pressure coefficient. |
| 37 | C_{p^*} | Reduced pressure coefficient. |
| 38 | f | Frequency. |
| 39 | H | Height of the low-rise building model, $H = 8$ cm . |
| 40 | I_u | Turbulence intensity of streamwise velocity component. |
| 41 | L_{ux} | Integral length scale of streamwise velocity component. |
| 42 | p | Pressure. |
| 43 | p_∞ | Ambient static pressure. |
| 44 | r | Radial distance on the xz -plane, i.e., $r = \sqrt{x^2 + z^2}$. |
| 45 | S_{uu} | Auto-spectra of streamwise velocity component. |
| 46 | u | Streamwise velocity component (with direction parallel to x -coordinate). |
| 47 | \mathbf{u} | Velocity vector, $\mathbf{u} = u\mathbf{i} + v\mathbf{j} + w\mathbf{k}$. |
| 48 | u_H | Upstream streamwise velocity at roof height. |
| 49 | u_{ref} | Reference velocity. |
| 50 | w | Vertical velocity component with direction parallel to z -coordinate. |
| 51 | x | x -coordinate of the space. |
| 52 | x_r | Reattachment length of the mean separation bubble. |
| 53 | \mathbf{x} | Space vector. $\mathbf{x} = x\mathbf{i} + y\mathbf{j} + z\mathbf{k}$ |
| 54 | z | Vertical coordinate of the space. |
| 55 | ν | Kinematic viscosity of air. |
| 56 | α | Coefficient associated with x -derivative of the analytic support, Φ . |
| 57 | β | Coefficient associated with z -derivative of the analytic support, Φ . |
| 58 | Φ | Analytic support. |
| 59 | ρ | Density of air. |
| 60 | σ | Support size of the radial analytic function Φ . |
| 61 | $\boldsymbol{\tau}$ | Turbulence stress tensor with component $\tau_{ij} = \overline{u_i' u_j'}$ |
| 62 | \bar{a} | Time average of a . |
| 63 | a' | Temporal fluctuation of a , i.e., $a' = a - \bar{a}$. |
| 64 | $\min(a)$ | Minimum value of a . |
| 65 | $\max(a)$ | Maximum value of a . |
| 66 | | |
| 67 | | |

68 1. Introduction

69 Free-stream turbulence is known to affect the mean flow around two-dimensional (2D)
70 rectangular prisms. For the separated and reattached flow near the leading edge, investigations
71 over several decades (e.g., Kiya and Sasaki, 1984; Saathoff and Melbourne, 1997) have shown
72 that increased free-stream turbulence intensity reduces the mean separation bubble length, x_r , on
73 both the upper and lower surfaces. On the other hand, altering the length scale of turbulence has
74 not been found to affect the length of the separation bubble as significantly as turbulence
75 intensity (e.g., Hillier and Cherry, 1981; Nakamura and Ozono, 1987), at least over the range
76 examined.

77 These findings have significant implications for the separated and reattached flow near a
78 low-rise building roof, where large suction can induce uplift failures in high winds. In order to
79 investigate the influence of turbulence in the atmospheric boundary layer (ABL), Akon and
80 Kopp (2016) conducted roof surface pressure measurements of a geometrically-scaled, low-rise
81 building together with planar particle image velocimetry (PIV) measurements in a boundary
82 layer wind tunnel. Near the height of the building, the turbulence intensity in their simulated
83 ABLs ranged from 10% to 30% while the integral length scale ranged from 6 to 12 times of
84 building height. Note that the turbulence intensity is defined as $I_u = \sqrt{\overline{u'u'}}/\bar{u}$, while the integral
85 length scale is defined as $L_{ux} = \bar{u} \int_0^\infty \overline{u'(t)u'(t+t_*)}/\overline{u'u'} dt_*$, where \bar{u} is the mean stream-wise
86 velocity, u' is the fluctuating component, t denotes time and t_* is the time lag. The general
87 effects of turbulence intensities and length scales on the mean reattachment length on the upper
88 surface of the roof was found to be similar to the cases for 2D rectangular prisms. The
89 distributions of mean pressure coefficients, $\overline{C_p}$, on the roof surface were found to be primarily
90 dependent on the reattachment length, x_r , but also on the turbulence intensity. The minimum
91 value of the mean pressure coefficient, $\min(\overline{C_p})$, was found to asymptotically decrease for
92 increased turbulence intensity. By further plotting the reduced mean pressure coefficients,
93 $C_p^* = (\overline{C_p} - \min(\overline{C_p})) / (1 - \min(\overline{C_p}))$, as originally defined by Roshko and Lau (1965), against the
94 normalized distance from the roof leading edge, x/x_r , they found that the mean pressure
95 distributions beneath the separated flow are not self-similar because of the dependence on the

96 turbulence intensity, I_u . In particular, they found that the value of Cp^* decreases at the
 97 reattachment point, $x/x_r = 1$, for increased values of I_u , indicating that the pressure takes
 98 relatively longer to recover with respect to the reattachment point (which decreases for increased
 99 values of I_u).

100 With the capability of PIV measurements, our goal now is to look into the more detailed
 101 influences of ABL turbulence on the flow field variation near the roof. From the Navier-Stokes
 102 equations, the flow field can be directly connected to the pressure field so that the influence of
 103 turbulence on the pressure field can be examined. By defining the pressure coefficient, Cp , as

$$104 \quad Cp = \frac{p - p_\infty}{0.5 \rho u_{ref}^2}, \quad (1)$$

105 and normalizing the velocity vector, \mathbf{u} , by the reference velocity, u_{ref} , the gradient of the mean
 106 pressure coefficient can be written as:

$$107 \quad \nabla \overline{Cp} = -2 \left[\left(\frac{\overline{\mathbf{u}}}{u_{ref}} \right) \cdot \nabla \left(\frac{\overline{\mathbf{u}}}{u_{ref}} \right) + \nabla \cdot \left(\frac{\overline{\boldsymbol{\tau}}}{u_{ref}^2} \right) - \frac{\nu}{u_{ref}} \nabla^2 \left(\frac{\overline{\mathbf{u}}}{u_{ref}} \right) \right]. \quad (2)$$

108 Here ρ denotes the density of the air, p denotes the pressure, p_∞ is the ambient static pressure
 109 and ν is the kinematic viscosity. The overbars in Eq. (2) denote the time average, while $\boldsymbol{\tau}$
 110 denotes the turbulent stress tensor with components $\tau_{ij} = \overline{u_i' u_j'}$ with the prime denoting a
 111 fluctuating component.

112 This Eulerian approach to pressure gradient evaluation, along with methods of pressure
 113 integration have been explored by many researchers and is recently reviewed by van
 114 Oudheusden (2013). The central difference scheme, which is of second order accuracy and
 115 relatively simple in operation, is usually used in determining the velocity gradients on the right
 116 hand side of Eq. (2) (e.g., Murai et al., 2007; de Kat and van Oudhuesden, 2012). On the side of
 117 pressure integration, however, greater attention is needed. Space-marching techniques for
 118 pressure integration are relatively straightforward and fast (e.g., Baur and Köngeter, 1999; van
 119 Oudheusden et al., 2007). However, at times ‘memory’ effects of integrated results along the
 120 integration path can occur (e.g., de Kat et al. (2008)), which means the pressure integration can
 121 be path dependent with errors from either discretization or measurement (e.g., Sciacchitano and
 122 Wieneke, 2016) being accumulated along the integration path (Ettl et al., 2008). Because of
 123 these drawbacks for space-marching schemes, other types of optimization methods for pressure

124 integration may be preferable. The most common approach is to solve the Poisson equation for
125 pressure with standard numerical techniques (e.g., Gurka et al., 1999; de Kat and van
126 Oudheusden, 2012). Note that boundary conditions of mixed type, i.e., a combination of
127 Dirichlet and Neumann, are required for solving Poisson equations (van Oudheusden, 2013). In
128 addition to these techniques, algorithms in CFD have also been used to determine pressure from
129 measured velocity data. For example, Jaw et al. (2009) calculated the pressure distribution
130 through the SIMPLER algorithm, in which continuity is satisfied and no boundary conditions are
131 required. In contrast to these methods, in the current work we are applying the analytic
132 interpolation approach proposed by Ettl et al. (2008). The goal of this method is to keep the
133 local details of integration while providing a globally optimized solution. This method has other
134 advantages, such as no requirements for entire boundary conditions and the ability to remove bad
135 gradient data.

136 An overview of this paper is as follows. The planar PIV and surface pressure measurements
137 of the flow fields around a low-rise building under various terrain roughness conditions, as
138 measured by Akon and Kopp (2016), are used as the input for analytic interpolation technique.
139 Following a description of the method, the mean pressure fields are obtained from the measured
140 mean velocity fields. The roof surface pressures estimated from velocity fields are then
141 compared to the measurements. Effects of turbulence in the ABL on the mean roof surface
142 pressure distributions are, hence, examined directly.

143

144

145 **2. Atmospheric boundary layer (ABL) flow simulation with various terrain roughness** 146 **conditions**

147 Six upstream terrain conditions were used for generating the turbulent atmospheric boundary
148 layer (ABL) flows. While the measurements are briefly reviewed here, full details can be found
149 in Akon and Kopp (2016). These ABL turbulent flows are simulated in the high-speed test
150 section of Boundary Layer Wind Tunnel II at the University of Western Ontario (UWO), which
151 offers a fetch of 39 m for flow development and a cross-section of 3.36 m in width and 2.05 m in
152 height at the test location. At the upstream end, three spires, with a height of 1.22 m and a base
153 width of 0.1 m, are placed. Sets of roughness blocks are distributed along the floor between the
154 upstream end and the test location. By altering the heights of the roughness blocks, three distinct

155 ABL turbulent flows, which are called ‘Flat’, ‘Open’ and ‘Suburban’ in this paper, are generated.
 156 By further placing a barrier of 0.38 m (15 inch) height immediately after the spires, along with
 157 the same sets of roughness blocks mentioned earlier, another three sets of ABL flow are
 158 generated with altered integral scales. In summary, the measurements were conducted with a
 159 total of six terrain roughness conditions. Three of them, with 15 inch barrier at the upstream end,
 160 are labelled as ‘F15’, ‘O15’ and ‘S15’ for Flat, Open and Suburban roughness distributions,
 161 respectively; the remaining three, without upstream barriers, are labelled as ‘F0’, ‘O0’ and ‘S0’,
 162 correspondingly.

163 In order to measure characteristic profiles of the simulated ABL turbulent flows, four-hole
 164 Cobra probes (TFI Inc., model no. 900) were used. The working principles for velocity
 165 measurements using these probes can be found on the manufacturer’s website (TFI Inc., 2017).
 166 The Cobra probes used were calibrated by the manufacturer, which were verified by comparisons
 167 with Pitot-static probes in low turbulence flow. Akon (2017) assessed the measurement
 168 uncertainty as 2.3%. Vertical profiles of the mean longitudinal velocity component, \bar{u} , are
 169 normalized by the mean longitudinal velocity at the roof height, i.e., \bar{u}/\bar{u}_H , two of which are
 170 shown in Figures 1(a-b) as a function of normalized height, z/H . Here, z denotes the vertical
 171 distance from the wind tunnel floor and $H = 0.08$ m is the building height of the (geometrically-
 172 scaled) model. Near the roof, i.e., $z/H \leq 3$, similar vertical distributions of \bar{u}/\bar{u}_H can be found
 173 for the Flat and Open terrains (i.e., ‘F0’, ‘F15’, ‘O0’ and ‘O15’) while a significant increase of
 174 shear is observed in the Suburban terrains (i.e., ‘S0’ and ‘S15’). The ratios of building height to
 175 roughness length, known as the Jensen number, are 540, 600, 290, 600, 56 and 71 for terrains
 176 ‘F0’, ‘F15’, ‘O0’, ‘O15’, ‘S0’ and ‘S15’ respectively, as reported by Akon and Kopp (2016).

177 Figure 1(c) shows the vertical profiles for the turbulence intensities, $I_u = \sqrt{\overline{u'u'}}/\bar{u}$, in each of the
 178 six terrains. Clear increases in turbulence intensities can be observed for increased roughness
 179 along the wind tunnel floor. Adding the 15-inch barrier at the upstream end has less effect on
 180 turbulence intensity. Hence, the relative intensity of turbulence near the roof height can be a
 181 summarized as $I_{u,F0} \cong I_{u,F15} < I_{u,O0} \cong I_{u,O15} < I_{u,S0} < I_{u,S15}$, where the terrains are labelled in the
 182 subscripts.

183 The power spectral densities of the longitudinal velocity fluctuations were also obtained at

184 the roof height for the six terrains. Instead of using the typical normalization, $fS_{uu}/\overline{u'u'}$, for the
185 spectra, we have non-dimensionalized them as fS_{uu}/\overline{u}^2 , where f denotes the frequency and
186 S_{uu} is the autospectral density. This normalization is similar to the conventional one but with
187 additional information on turbulence intensity, since $\int_{f=0}^{\infty} S_{uu}/\overline{u}^2 df$ is in fact equal to I_u^2 . So, the
188 clear increases of turbulence intensity due to increased roughness that are observed in Figure 1(c)
189 are reflected in the magnitude changes in the reduced spectra in Figure 1(d). In addition to the
190 magnitude of the fluctuations, the associated length scales can also be observed for the six
191 upstream turbulence conditions. The reduced spectra obtained from F15 and O15 generally shift
192 the F0 and O0 counterparts toward the larger length scale side (Figure 1(d)). However, S15
193 terrain not only produces more large scale turbulence but maintains the smaller scale turbulence
194 equivalent to S0, leading to total increase of turbulence intensity shown in Figure 1(c). Akon and
195 Kopp (2016) reported the ratios of integral length scales to building height, L_{ux}/H , as being 6,
196 8, 7, 13, 11 and 12 for terrains F0, O0, S0, F15, O15 and S15, respectively, where the integral
197 length scale is defined as $L_{ux} = \overline{u} \int_0^{\infty} \overline{u'(t)u'(t+t_*)}/\overline{u'u'} dt_*$. The vertical distributions of L_{ux} are
198 found to be nearly uniform for the region close to the roof. Hence, the terrains with the 15-inch
199 barrier at the upstream end produce turbulent flows of larger length scales as compared to
200 terrains without the barrier. Note that these ABL flows produced from the six sets of terrain
201 roughness are generally applicable for wind tunnel simulation of the real wind environment
202 (Akon and Kopp, 2016).

203

204

205 3. PIV and pressure measurement on a low-rise building model

206 The Time-Resolved Particle Image Velocimetry (TR-PIV) measurements, synchronized with
207 surface pressure measurements, were taken by Akon and Kopp (2016) on a 1/50 scaled model of
208 Texas Tech University's Wind Engineering Research Field Laboratory (WERFL) Building
209 (Levitan and Mehta, 1992). These data were utilized in the present study. The modelled
210 building has plan dimensions of 18.3 cm \times 27.5 cm with a height of 7.8 cm (see Figure 2). Nine
211 pressure taps were placed along the centreline of the model roof surface to facilitate the pressure

212 measurements. The pressure coefficients have an absolute measurement uncertainty of about 0.1
213 on C_p values (Quiroga, 2006).

214 The TR-PIV system, used by Akon and Kopp (2016), uses two 1Mb Photron FASTCAM-
215 1024 PCI CMOS cameras. A time delay of 85 micro-seconds was applied between the two
216 images of a single image pair. The TR-PIV measurements of the velocity field (sampling
217 frequency of 500 Hz) synchronized with roof-surface pressure measurements (sampling
218 frequency of 1108 Hz) were taken for a duration of 160 seconds for each of the six upstream
219 flow conditions. A detailed discussion on the TR-PIV system, and the synchronization of the
220 pressure and velocity measurements can be found in Taylor et al. (2010). Interrogation windows
221 of 32×32 pixels with 50% overlap were used during processing the PIV raw images in TSI
222 Insight 4G utilizing an FFT cross-correlation algorithm. Standard cross-correlation algorithms
223 have a spatial uncertainty of less than approximately 0.1 pixels (Huang et al., 1997). The final
224 grid spacing between data points is $\Delta x = \Delta z = 0.2$ cm for upstream field of view (i.e., FOV 1 in
225 Figure 2) and $\Delta x = \Delta z = 0.18$ cm for rooftop field of view (i.e., FOV 2 in Figure 2). The
226 Cartesian coordinate system used in current analyse is also attached in Figure 2. A detailed
227 explanation of the experimental procedure can be found in Akon and Kopp (2016).

228 The PIV data are compared to the Cobra probe data in Figures 1(a-b) for the mean profiles,
229 and in Figure 1(c) for the turbulence intensity profiles. These figures indicate that there is an
230 excellent match between the mean profiles, while there are differences in the turbulence
231 intensities of up to 0.02 – 0.03, which can be explained by the measurement uncertainty.

232

233

234 **4. Integration of planar pressure gradient data using the analytic interpolation technique**

235 The analytic interpolation technique proposed by Ettl et al. (2008) for surface reconstruction
236 is explained and applied for integrating mean pressure gradient data in this section. The Navier-
237 Stokes equations, represented in Eq. (2), are used to determine the mean pressure gradient using
238 planar PIV measurement data. For wind normal to the building and a measurement plane on the
239 centerline, the mean flow field can be treated as symmetric and, hence, the gradients associated
240 with out-of-plane component are negligible. The exact components used in Eq. (2) for
241 evaluation of mean pressure gradient are:

$$242 \quad \frac{\partial \overline{Cp}}{\partial x} = -2 \left[\frac{\bar{u}}{u_{ref}} \frac{\partial}{\partial x} \left(\frac{\bar{u}}{u_{ref}} \right) + \frac{\bar{w}}{u_{ref}} \frac{\partial}{\partial z} \left(\frac{\bar{u}}{u_{ref}} \right) + \frac{\partial}{\partial x} \left(\frac{u' u'}{u_{ref}} \right) + \frac{\partial}{\partial z} \left(\frac{u' w'}{u_{ref}} \right) - \nu \left(\frac{\partial^2}{\partial x^2} \left(\frac{\bar{u}}{u_{ref}} \right) + \frac{\partial^2}{\partial z^2} \left(\frac{\bar{u}}{u_{ref}} \right) \right) \right] \quad (3a)$$

$$243 \quad \frac{\partial \overline{Cp}}{\partial z} = -2 \left[\frac{\bar{u}}{u_{ref}} \frac{\partial}{\partial x} \left(\frac{\bar{w}}{u_{ref}} \right) + \frac{\bar{w}}{u_{ref}} \frac{\partial}{\partial z} \left(\frac{\bar{w}}{u_{ref}} \right) + \frac{\partial}{\partial x} \left(\frac{u' w'}{u_{ref}} \right) + \frac{\partial}{\partial z} \left(\frac{w' w'}{u_{ref}} \right) - \nu \left(\frac{\partial^2}{\partial x^2} \left(\frac{\bar{w}}{u_{ref}} \right) + \frac{\partial^2}{\partial z^2} \left(\frac{\bar{w}}{u_{ref}} \right) \right) \right] \quad (3b)$$

244 On the right-hand side of Eq. (3), the 1st and 2nd terms are associated with the mean convection,
 245 the 3rd and 4th terms are associated with turbulence, and the 5th and 6th terms are associated with
 246 viscous stresses.

247 The analytic interpolation approach developed by Ettl et al. (2008) offers an effective tool for
 248 topological surface reconstruction by integrating measured gradient data. Because the
 249 differential momentum equation offers gradient information of pressure, as shown in Eq. (3), the
 250 reconstruction method of Ettl et al. (2008) will be applicable to pressure reconstruction. In this
 251 approach, the estimated pressure coefficient, Cp_e , at location \mathbf{x} is assumed as a linear spatial
 252 superposition of analytic functions, i.e.,

$$253 \quad Cp_e(\mathbf{x}) = \sum_{j=1}^N \left[\alpha_j \frac{\partial}{\partial x} \Phi(\mathbf{x} - \mathbf{x}_j) + \beta_j \frac{\partial}{\partial z} \Phi(\mathbf{x} - \mathbf{x}_j) \right], \quad (4)$$

254 where α_j and β_j are the appropriate coefficients for the x and z derivatives of analytic support
 255 centred at the j -th grid point, respectively; N denotes total number of grid points. Wenland's
 256 function was selected by Ettl et al. (2008), and is also used here for the analytic support, Φ .
 257 This function is symmetric about its centre and resembles a bell-shaped surface for the radial
 258 distance $r \leq 1$ and is zero for regions of $r > 1$, i.e.,

$$259 \quad \Phi(r) = \begin{cases} \frac{1}{3} (1-r)^6 (35r^2 + 18r + 3) & \text{for } r \leq 1 \\ 0 & \text{for } r > 1 \end{cases} \quad \text{with } r = \sqrt{x^2 + z^2}. \quad (5)$$

260 The support size, which is denoted as σ , describes the range of influence of the radial support
 261 Φ . As can be seen in Eq. (5), the support size is unity for the original Wenland's function.
 262 Adjustment of the support size may be needed in order to render smooth integration results for
 263 various grid spacings. Such adjustment can be simply achieved by replacing original grid
 264 location, \mathbf{x} , in Eq. (4) by the normalized one, \mathbf{x}/σ . Thus, the $Cp_e(\mathbf{x})$ in Eq. (4) is directly
 265 related to j -th support if $|\mathbf{x} - \mathbf{x}_j| \leq \sigma$, while supports outside the influence region can be
 266 neglected in Eq. (4). In order to determine the coefficients α and β , the gradient of Cp_e

267 represented by Eq.(4) is taken at grid point \mathbf{x}_i and matched with the measured gradient data
 268 obtained from the Navier-Stokes equations, Eq.(3), such that

269

$$\underbrace{\begin{bmatrix} \frac{\partial^2}{\partial x^2} \Phi(\mathbf{x}_i - \mathbf{x}_j) & \frac{\partial^2}{\partial x \partial z} \Phi(\mathbf{x}_i - \mathbf{x}_j) \\ \frac{\partial^2}{\partial x \partial z} \Phi(\mathbf{x}_i - \mathbf{x}_j) & \frac{\partial^2}{\partial z^2} \Phi(\mathbf{x}_i - \mathbf{x}_j) \end{bmatrix}}_{\mathbf{A}, 2N \times 2N} \underbrace{\begin{bmatrix} \alpha_j \\ \beta_j \end{bmatrix}}_{\mathbf{c}, 2N \times 1} = \underbrace{\begin{bmatrix} \frac{\partial}{\partial x} \overline{Cp}(\mathbf{x}_i) \\ \frac{\partial}{\partial z} \overline{Cp}(\mathbf{x}_i) \end{bmatrix}}_{\mathbf{d}, 2N \times 1}. \quad (6)$$

270

271
 272 Once the linear system described in Eq.(6) is established, the coefficients can be solved by
 273 matrix inversion.

274 There are a few notes regarding the application. First, since the integration scheme is based
 275 on gradient data, the integrated values resulting from Eq.(4) only offer information of relative
 276 difference. Therefore, it is necessary to specify a constant of integration at a specified location
 277 within the domain of measurement. Second, if a normalized grid location, \mathbf{x}/σ , is used in Eq.
 278 (4), the measured gradient data must be pre-multiplied by σ before putting into vector \mathbf{d} in
 279 Eq.(6), in order to account for the chain rule.

280 The current interpolation method allows users to treat bad data points with two options
 281 because of the advantages of the mathematical nature of Eq. (4). Within the measurement plane,
 282 assume that there are bad gradient data points scattered at locations \mathbf{x}_b , which have a total
 283 number of N_b . The first option is to exclude the radial basis supports located at \mathbf{x}_b in Eq. (4)
 284 but keep full gradient data in \mathbf{d} in Eq. (6). In this case, \mathbf{A} becomes a non-square matrix of
 285 dimension $2N \times 2(N - N_b)$ and \mathbf{d} is still a vector of dimension $2N \times 1$. Then, a least-squares
 286 method can be used to solve for the coefficient vector \mathbf{c} in Eq. (6), as mentioned in Ettl et al.
 287 (2008). The second option is to remove both the supports at \mathbf{x}_b in Eq. (4) and bad gradient data
 288 in vector \mathbf{d} in Eq. (6). The corresponding dimensions of matrices \mathbf{A} and \mathbf{d} have sizes of
 289 $2(N - N_b) \times 2(N - N_b)$ and $2(N - N_b) \times 1$, respectively, in this case. Therefore, direct matrix
 290 inversion can be used again to solve the coefficient vector. The reconstruction at bad gradient
 291 data locations can then be treated as extrapolation by simply evaluating $Cp_e(\mathbf{x}_b)$ in Eq. (4).
 292 Interested readers are referred to Ettl et al. (2008) for more useful techniques for application.

293 A review of the details used in current pressure integration is as follows. Once the mean
294 velocities and turbulence stresses are captured from the two PIV FOV's in Figure 2, they are
295 normalized by reference velocity, u_{ref} , for calculation of Eq. (3). The reference velocity used
296 throughout this paper is defined as mean streamwise velocity at roof height and an upstream
297 location where no influences of building are expected, i.e., $u_{ref} = \bar{u}_H$. (It should be noted that the
298 region of influence is at least $2H$ upstream of the building, which is not captured by the images
299 in Figure 3.) The central difference scheme is applied to calculate the pressure gradient vectors
300 according to differential momentum in Eq. (3). Bad pressure gradient data are identified and
301 removed in the reconstruction process if the magnitude is two times larger or the direction
302 deviates 120° from the averaged value obtained from its eight immediate neighbors. The bad
303 pressure gradient data are mainly located near the model surface due effects of laser reflection.
304 The maximum number of the bad data points is fewer than 2% of the data points within the two
305 fields of view. The size of the analytic support is chosen to be about 14 times that of the PIV
306 data grid spacing in order to render reconstruction smoothness.

307 The integration process is first conducted for FOV 1 by using the gradient information
308 measured in this FOV. The mean pressure is assumed to be the same as the ambient value, i.e.,
309 $\overline{Cp} = 0$, at the upstream, higher corner of FOV 1, i.e., $\{x = -1.5H, z = 1.75H\}$. This assumption
310 is based on zero pressure gradient in the vertical direction in boundary layer equation (e.g.,
311 Wilcox, 2007) for upstream flow where the interference of the model is minimal (e.g., Peren et
312 al., 2015). Following a similar approach but assuming an arbitrary initial integration constant,
313 the pressure field can also be integrated for FOV 2. The reconstructed pressures in FOV 2 are
314 then adjusted by an integration constant such that the difference of the area-averaged pressures
315 within the overlap region between FOV's 1 and 2 (see Figure 2) is zero. Note that such
316 procedure in fact minimizes the difference of integrated pressures within the overlapped region
317 between FOV's 1 and 2 (Ettl et al., 2008).

318

319

320 5. Results and discussion

321 5.1. Convection terms

322 Planar PIV measurements were conducted near the building roof under the six upstream terrain
323 conditions mentioned in Section 2. Figure 3 shows the ratio of the mean velocity magnitude, $|\bar{\mathbf{u}}|$,
324 to a reference velocity, u_{ref} , for all six terrains. Generally, a speed-up ratio of about 1.4 can be
325 found when comparing the mean upstream velocity at the roof height, and about $0.5H$ upstream
326 of the building, to the velocity above the top of the roof on the same streamline. Low velocities
327 can be found within the stagnation region in front of the wall and in the recirculation region
328 above the roof. The contribution of the convection terms to the pressure gradient in the Navier-
329 Stokes equations, i.e., the 1st and 2nd terms on the right-hand side of Eq. (3), is shown in Figure 4
330 for all six upstream terrain conditions. Generally, the gradient vectors are found to radiate from
331 the windward corner, with the magnitudes being the largest near the leading edge and reduced
332 above the mean separation bubbles (which are also shown in Figure 4). Over the regions farther
333 away from the leading edge and within the separation bubbles, relatively small gradient vectors
334 can be observed.

335 As already noted by Akon and Kopp (2016), the size of separation bubbles is much more
336 sensitive to the intensity than the scale of the upstream turbulence, being smaller for greater
337 values of turbulence intensity. Their observation can be easily verified by reviewing the
338 turbulence intensities in Figure 1(c) and the mean separation bubbles in Figure 4. Because the
339 curvature of the streamlines increases as the size of separation bubbles is reduced, the
340 convection-contributed pressure gradients above the separation bubbles are intensified for
341 rougher terrains. The terrain effects on relative mean velocity magnitude (see Figure 3) are not
342 significant in general, although details of velocity variation near the leading edge are different
343 when comparing the results in Figure 3 for terrains ‘F0’ and ‘S15’. Lower velocity magnitude
344 variation near the leading edge can be found for terrain ‘F0’ while higher variation can be
345 observed for terrain ‘S15’. The more rapid spatial variations of velocity magnitude increases the
346 convection-contributed pressure gradients as well, so that the pressure gradients of terrain ‘S15’
347 are larger than that in terrain ‘F0’ near the leading edge (see Figure 4).

348

349

350 5.2. Turbulence terms

351 The three distinct components of turbulence stress tensors, $\overline{u'u'}$, $\overline{w'w'}$ and $\overline{u'w'}$, are
352 normalized by reference velocity and shown respectively in Figures 5, 6 and 7. Once these
353 turbulence stresses are measured, the turbulence contribution to the mean pressure gradient
354 vectors, which is shown in Figure 8, can be obtained by evaluating the 3rd and 4th terms of Eq.
355 (3). For the distribution of $\overline{u'u'}/u_{ref}^2$, shown in Figure 5, maximum values are found to coincide
356 with the shear layer region while decreasing values can be found for the regions away from the
357 shear layers. By further comparing Figure 5 to Figures 6 and 7, it is observed that the $\overline{u'u'}$
358 component dominates the turbulence stress tensor, with maximum magnitudes around 4 times
359 that of the other two. Hence, according to Eq. (3a), the turbulence-contributed pressure gradient
360 vectors generally radiate from the shear layer in a nearly horizontal direction. For the
361 distribution of $\overline{w'w'}/u_{ref}^2$ shown in Figure 6, larger magnitudes are found over the leeward half
362 of the separation bubbles. The spatial variation of $\overline{w'w'}/u_{ref}^2$ is responsible for the pressure
363 gradients in the vertical direction, according to Eq. (3b). For the distribution of $\overline{u'w'}/u_{ref}^2$ shown
364 in Figure 7, a spatial migration of the positive peaks near the roof leading edge to the negative
365 peaks over the leeward half of the separation bubbles can be found. According to Eq. (3), the
366 vertical gradient of $\overline{u'w'}/u_{ref}^2$ is associated with the horizontal pressure gradient while the
367 horizontal gradient of $\overline{u'w'}/u_{ref}^2$ is associated with the vertical pressure gradient.

368 The effects of upstream terrain conditions on the turbulence-contributed pressure gradients
369 are described here. As shown in Figure 5, the maximum values of $\overline{u'u'}/u_{ref}^2$ increase as the
370 intensity or length scale of the upstream turbulence increases. However, the influence of
371 turbulence intensity is more significant than length scale. In particular, increasing $(I_u)^2$ in the
372 upstream flow by a factor of four (i.e., doubling the turbulence intensity upstream) doubles the
373 maximum values of $\overline{u'u'}/u_{ref}^2$ (or, taking the square root, the turbulence intensity above the roof
374 by 40%; compare the Flat and Suburban terrains in Figure 5), while doubling L_{ux} only increase
375 the maximum $\overline{u'u'}/u_{ref}^2$ by around 20% (or a 10% increase in the intensity above the roof; see
376 terrains with and without the 15-inch barrier in Figure 5). For the $\overline{u'w'}/u_{ref}^2$ distribution shown
377 in Figure 7, higher positive peak values are found for higher upstream turbulence intensity, while

378 negative peak values appear to be mostly independent from the terrain effects. However, the
379 distances between the high and low peak values of $\overline{u'w'}/u_{ref}^2$ shrink as the sizes of separation
380 bubbles reduce. For the distribution of $\overline{w'w'}/u_{ref}^2$ shown in Figure 6, reduced effects of the
381 upstream terrain conditions can be observed. As a result of these variations, larger turbulence-
382 contributed pressure gradients can be found for higher upstream turbulence intensities, for
383 regions near the shear layers and roof surface, as shown in Figure 8. The effects of the turbulence
384 length scales are observed to be less significant.

385
386

387 5.3. Total pressure gradients

388 For high Reynolds number flow, the viscosity contribution is relatively small (e.g., van
389 Oudheusden et al., 2007). The contribution of the viscosity terms to the final integrated
390 pressures are less than 1% for all the cases with the current measurements. By summing the
391 contributions of convection, turbulence and viscosity in the Navier-Stokes equations, the total
392 gradient of \overline{Cp} can be obtained, and is shown in Figure 9 for each of the six terrains.

393 By assuming that the viscosity contribution is negligible, the vector contributions of the
394 convection-contributed pressure gradient, $(\nabla\overline{Cp})_{conv}$, and turbulence-contributed pressure
395 gradient, $(\nabla\overline{Cp})_{turb}$, to the total pressure gradient, $(\nabla\overline{Cp})_{total}$, are schematically shown in Figure
396 10(a). In order to quantify the contributions, the projections of each term onto the total gradient
397 are normalized by the magnitude of total gradient. For example, the vector contribution of the
398 convection term can be formulated as follows:

$$399 \frac{|(\nabla\overline{Cp})_{conv}| \cos \theta_{conv}}{|\nabla\overline{Cp}_{total}|} = \frac{(\nabla\overline{Cp})_{conv} \cdot (\nabla\overline{Cp})_{total}}{|\nabla\overline{Cp}_{total}|^2}, \quad (7)$$

400 where θ_{conv} is the angle between $(\nabla\overline{Cp})_{conv}$ and $(\nabla\overline{Cp})_{total}$, as defined in Figure 10(a). For the
401 convenience of calculation, the vector contribution defined on the left-hand side of Eq. (7) can be
402 represented as the inner product between $(\nabla\overline{Cp})_{conv}$ and $(\nabla\overline{Cp})_{total}$, as shown on the right-hand
403 side of the same equation.

404 Preliminary calculation of the vector contribution using Eq. (7) shows similar pattern for all
 405 six upstream terrain conditions. Hence, only the results obtained from terrain O15 are shown
 406 here. As can be clearly seen in Figure 10(b), the convection term governs the total pressure
 407 gradient in the region above the separation bubbles and away from the building surface, for more
 408 than 90% of the total. On the other hand, the turbulence contribution shown in Figure 10 (c)
 409 governs the region within the separation bubbles, with maximum contribution of more than 90%
 410 near the roof surface along the leeward side of the separation bubbles.

411
 412

413 5.4. Integrated pressure field

414 The analytic interpolation technique introduced in Section 4 is applied to integrate the total
 415 mean pressure gradients shown in Figure 9. The reconstructed \overline{Cp} fields are shown in Figure 11
 416 for the six terrain conditions. Smooth distributions of the integrated \overline{Cp} 's can be observed for
 417 all terrains, with the lowest negative values centered at the windward portion of the mean
 418 separation bubbles (see Figure 4). For locations far upstream of the building, relatively little
 419 variation of integrated pressures can be observed. Hence, by assuming that the pressure at an
 420 upstream point is equivalent to the ambient pressure, Bernoulli's equation, i.e.,

$$421 \quad \overline{Cp}_{\text{roof top}} = \overline{Cp}_{\text{upstream}} + \frac{|\overline{\mathbf{u}}_{\text{upstream}}|^2}{u_{\text{ref}}^2} - \frac{|\overline{\mathbf{u}}_{\text{roof top}}|^2}{u_{\text{ref}}^2}, \quad (8)$$

422 can also be applied to evaluate the pressure along the streamlines and, therefore, serve as a
 423 crosscheck for the integrated results. In Eq. (8), $\overline{Cp}_{\text{upstream}}$ and $\overline{\mathbf{u}}_{\text{upstream}}$ denote, respectively, the
 424 mean pressure coefficients and velocity at an upstream location for the selected streamline, while
 425 $\overline{Cp}_{\text{roof top}}$ and $\overline{\mathbf{u}}_{\text{roof top}}$ denote, respectively, the mean pressure coefficient and velocity at a
 426 downstream location above the roof on the same streamline. Two streamlines are selected, in
 427 terrains 'F0' and 'S15', for this purpose (see Figures 8 and 11): The upper streamline starts at an
 428 upstream point near $\{x = -H; y = 1.375H\}$ while the lower one starts at an upstream point near
 429 $\{x = -H; y = 0.75H\}$. Figure 12 shows the comparison of Bernoulli-estimated \overline{Cp} 's to the
 430 integrated results extracted from the upper and lower streamlines in Figure 11. Good agreement
 431 of \overline{Cp} 's can be found between Bernoulli's estimations and integrated results for the upper

432 streamlines under the two selected terrain conditions. Such agreement manifests the
 433 applicability of the analytic interpolation technique for pressure reconstruction introduced in
 434 Section 4. However, for the lower streamlines in both terrains, Bernoulli's equation begins to
 435 undershoot the suction at $\{x/H \approx 0.25\}$ and continues accumulating the underestimation for the
 436 rest of downstream region. Such accumulating underestimation of Bernoulli's equation is due to
 437 the absence of the turbulence-contributed pressure gradients near the separated shear layers. By
 438 reviewing the sub-plots in Figure 8 for terrains 'F0' and 'S15', both of the lower streamlines are
 439 found to enter the region of large turbulence-contributed pressure gradients near $\{x/H \approx 0.25\}$.
 440 Because these turbulence-contributed pressure gradient vectors point in the direction opposite to
 441 the flow direction, the missing accumulation of these vectors along the positive flow direction
 442 leads to an underestimation of Bernoulli-estimated $\overline{C_p}$'s along the lower streamlines.

443

444

445 5.5. Surface pressures

446 The mean roof surface pressure coefficients measured by Akon and Kopp (2016) are shown
 447 in Figure 13 for six upstream terrain conditions and compared to the integrated $\overline{C_p}$'s extracted
 448 from a horizontal line near the roof height in Figure 11. As the upstream turbulence intensity
 449 increases, progressive variations of the $\overline{C_p}$ distributions can be observed in the roof surface
 450 pressure measurements. For terrains producing lower turbulence intensity, the $\overline{C_p}$ distributions
 451 resemble a plateau for the windward portion of the separation bubbles. As the upstream
 452 turbulence intensity increases, the plateau reduces to a prominent peak as a result of reduced size
 453 of the separation bubble. The minimum $\overline{C_p}$ can also be found to gradually decrease as the
 454 upstream turbulence intensity increases (Akon and Kopp, 2016). For example, the
 455 $\min(\overline{C_p}) = -0.9$ is observed for roof height $I_u = 13\%$ (see Figure 1 (b)) while $\min(\overline{C_p}) = -1.3$
 456 is observed for roof height $I_u = 27\%$. However, as the distance from the leading edge increases,
 457 these minimum $\overline{C_p}$'s gradually recover to a common value of $\overline{C_p} = -0.2$. Hence, higher rates
 458 of pressure recovery can be found for the rougher terrains that produce higher turbulence
 459 intensities. As discussed in the Introduction, because the $\overline{C_p}$ distributions are strongly

460 dependent on the sizes of the separation bubbles, Akon and Kopp (2016) also examined the
 461 universality of the mean pressure distributions by plotting Roshko and Lau's (1965) reduced
 462 form of mean pressure coefficients, i.e.,

$$463 \quad C_p^* = \frac{\overline{C_p} - \min(\overline{C_p})}{1 - \min(\overline{C_p})}, \quad (9)$$

464 against reduced distance, x/x_r . Here C_p^* denotes the reduced pressure coefficients and x_r
 465 denotes the reattachment length. From the results shown in Figure 14, Akon and Kopp (2016)
 466 found that, although the minimum mean pressures generally locate at $x/x_r = 0.25$ for these six
 467 terrains, the distribution of mean pressure coefficients is not self-similar.

468 The reconstructed field of $\overline{C_p}$'s are extracted from a horizontal line near roof height and
 469 compared to the roof surface measurements in Figure 13. Good agreement between the results
 470 obtained from the Navier-Stokes equations and the roof surface measurement can be observed
 471 for all six terrains, with maximum deviations in the magnitudes of $\max(|\Delta \overline{C_p}|)$ being less than
 472 0.1. This is consistent with the measurement uncertainty of the surface pressure measurements of
 473 about 0.1 (Quiroga, 2006). Hence, the variation in the mean pressure coefficients observed from
 474 surface measurements for the six terrains can be observed in the integrated results as well.

475 As the upstream turbulence intensity increases, the minimum $\overline{C_p}$ obtained from integration
 476 also decreases (see Figures 11 and 13). By reviewing what has been discussed so far, for the
 477 gradient fields of the mean pressures (i.e., Figure 9), the decreasing minimum mean pressure is
 478 due to the increased pressure gradient obtained from both the convection (Figures 4 and 10(b))
 479 and turbulence (Figures 8 and 10 (c)) terms in the Navier-Stokes equations of Eq. (3). Higher
 480 rates of pressure recovery can be found in the integrated results as well. However, the turbulence
 481 terms govern the pressure recovery for the region just above the roof (see Figures 8 and 10(c))
 482 and higher turbulence-contributed pressure gradients can be found in this region for the rougher
 483 terrains that produce higher turbulence intensities. These increased pressure gradients, which
 484 lead to both the decreased minimum value and higher recovery rate of mean pressure, can be
 485 further linked back to the flow fields. As mentioned earlier, the increased convection-
 486 contributed pressure gradient is attributed to the reduced size of separation bubble (Figure 4) and
 487 more rapid spatial variation of velocity magnitude near the leading edge (Figure 3). On the other

488 hand, the increased turbulence-contributed pressure gradients are attributed to the increased
489 spatial variation of $\overline{u'u'}/u_{ref}^2$ in Figure 5 and $\overline{u'w'}/u_{ref}^2$ in Figure 7. The summary of these
490 effects for both the mean velocity and turbulence fields explains the variation of the \overline{Cp}
491 distribution on the roof shown in Figures 13 and 14. However, the turbulence-induced pressure
492 gradients are not large enough to allow the reduced pressure coefficient distribution to be self-
493 similar (see Figure 14). As a result, the reduced pressure coefficient of Eq. (9) has a smaller
494 magnitude at the mean reattachment point, $x/x_r = 1$ for higher turbulence flows.

495

496

497 **6. Conclusions**

498 The effects of the atmospheric boundary layer (ABL) turbulence intensity and length scales
499 on the mean separated and reattached flow, and roof surface pressure were examined by Akon
500 and Kopp (2016). The goal of the current work is to extend the understanding of their
501 observations by further linking the velocity and turbulence fields to the pressure fields. The main
502 contributions and findings are summarized as follows.

- 503 (i) The Navier-Stokes equations are used to determine the gradient vectors of the mean
504 pressure field from the planar PIV data. The convection-contributed pressure gradients are
505 identified by evaluating the terms associated with mean velocities in the Navier-Stokes
506 equations. The turbulence-contributed pressure gradients, on the other hand, are identified
507 by terms associated with the Reynolds stresses. Effects of upstream turbulence on both of
508 the convection- and turbulence-contributed pressure gradients can, hence, be examined.
- 509 (ii) In order to obtain the pressure field from the velocity field, the analytical interpolation
510 technique of Ettl et al. (2008) is applied. The reconstructed pressure fields match
511 Bernoulli's equation well along a streamline away from the body and direct pressure
512 measurement on the surface of the body. Hence, the evaluation of pressure gradient using
513 the Navier-Stokes equations and the corresponding pressure integration technique are
514 validated.
- 515 (iii) Akon and Kopp (2016) found that the minimum mean roof surface pressure coefficient,
516 $\min(\overline{Cp})$, decreases for increased upstream turbulence intensity. In the current work, these

517 decreasing $\min(\overline{C_p})$'s are directly related to both increased convection- and turbulence-
518 contributed pressure gradients over the windward region of the mean separation bubbles.
519 (iv) As the upstream turbulence intensity increases, a more rapid pressure recovery can be
520 found for the portion of roof surface on the leeward side of the location of $\min(\overline{C_p})$. Such
521 increased surface pressure recovery rates are mainly due to the increased turbulence-
522 contributed pressure gradients near the roof surface. However, the rate of recovery is not
523 sufficiently high such the normalized pressure distribution is not self-similar.

524
525

526 **Acknowledgements**

527 This work was funded by the Natural Sciences and Engineering Research Council (NSERC)
528 of Canada under the Collaborative Research and Development (CRD) program and by the
529 Institute for Catastrophic Loss Reduction (ICLR).

530
531
532

533 **References**

534 Akon, A. F., Kopp, G. A., 2016. Mean pressure distributions and reattachment lengths for roof
535 separation bubbles on low-rise buildings. *J. Wind Eng. Ind. Aerodyn.* 155, 115-125. DOI:
536 10.1016/j.jweia.2016.05.008

537 Akon, A.F., 2017, Effects of turbulence on the separating-reattaching flow above surface-
538 mounted, three-dimensional bluff bodies. PhD thesis, The University of Western Ontario.

539 Baur, T., Königeter, J., 1999. PIV with high temporal resolution for the determination of local
540 pressure reductions from coherent turbulent phenomena. In: 3rd Int. Workshop on Particle
541 Image Velocimetry (Santa Barbara, USA, Sep. 16-18, 1999), 671-676.

542 de Kat, R., van Oudheusden, B. W., Scarano, F., 2008. Instantaneous planar pressure field
543 determination around a square-section cylinder based on time-resolved stereo-PIV. In: 14th
544 Int Symp. on Applications of Laser Techniques to Fluid Mechanics (Libson, Portugal, Jul. 7-
545 10, 2008). <http://ltces.dem.ist.utl.pt/lxaser/lxaser2008/programme.asp> (Last date of access:
546 Sep 1, 2017)

547 de Kat, R., van Oudheusden, B. W., 2012. Instantaneous planar pressure determination from
548 PIV in turbulent flow. *Exp. Fluids* 52 (5), 1089-1106. DOI: 10.1007/s00348-011-1237-5

549 Ettl, S., Kaminski, J., Knauer, M. C., Hüsler, G., 2008. Shape reconstruction from gradient
550 data. *Applied Optics*, 47 (12), 2091 - 2097. DOI: 10.1364/AO.47.002091

- 551 Gurka, R., Liberzon, A., Herfetz, D., Rubinstein, D., Shavit, U., 1999. Computation of pressure
552 distribution using PIV velocity data. In: 3rd Int. Workshop on Particle Image Velocimetry
553 (Santa Babara, USA, Sep. 16-18, 1999) 101-106.
- 554 Huang, H., Dabiri, D., Gharib, M., 1997. On errors of digital particle image velocimetry. *Meas.*
555 *Sci. Technol.* 8, 1427–1440. DOI: 10.1088/0957-0233/8/12/007
- 556 Hillier, R., Cherry, N. J., 1981. The effects of stream turbulence on separation bubbles. *J. Wind*
557 *Eng. Ind. Aerodyn.* 8 (1-2), 49–58. DOI: 10.1016/0167-6105(81)90007-6
- 558 Jaw, S. Y., Chen, J. H., Wu, P. C., 2009. Measurement of pressure distribution from PIV
559 experiments. *Journal of Visualization.* 12 (1), 27-35. DOI: 10.1007/BF03181940
- 560 Kiya, M., Sasaki, K., 1983. Free stream turbulence effects on a separation bubble. *J. Wind Eng.*
561 *Ind. Aerodyn.* 14 (1-3), 375–386. DOI: 10.1016/0167-6105(83)90039-9
- 562 Levitan, M. L., Mehta, K. C., 1992. Texas Tech field experiments for wind loads part 1:
563 building and pressure measuring system. *J. Wind Eng. Ind. Aerodyn.* 43 (1-3), 1565–1576.
564 DOI: 10.1016/0167-6105(92)90372-H
- 565 Murai, Y., Nakada, T., Suzuki, T., Yamamoto, F., 2007. Particle tracking velocimetry applied to
566 estimate the pressure field around a Savonius turbine. *Meas. Sci. Technol.* 18, 2491-2503.
567 DOI: 10.1088/0957-0233/18/8/026
- 568 Nakamura, Y., Ozono, S., 1987. The effects of turbulence on a separated and reattaching flow.
569 *J. Fluid Mech.* 178, 477-490. DOI: 10.1017/S0022112087001320
- 570 Peren, J. I., van Hooff, T., Ramponi, R., Blocken, B., Leite, B. C. C., 2015. Impact of roof
571 geometry of an isolated leeward sawtooth roof building on cross-ventilation: Straight,
572 concave, hybrid or convex? *J. Wind Eng. Ind. Aerodyn.* 145, 102–114. DOI:
573 10.1016/j.jweia.2015.05.014
- 574 Quiroga Diaz, P. S. 2006. Uncertainty analysis of surface pressure measurements on low-rise
575 buildings. Master's thesis, The University of Western Ontario
- 576 Roshko, A., Lau, J. C., 1965. Some observations on transition and reattachment of a free shear
577 layer in incompressible flow. In: *Proceedings of the Heat Transfer and Fluid Mechanics*
578 *Institute* (Charwat, A. F. ed.), 157–167. Stanford/CA: Stanford University Press.
- 579 Saathoff, P. J., Melbourne W. H., 1997. Effects of free-stream turbulence on surface pressure
580 fluctuations in a separation bubble. *J. Fluid Mech.* 337, 1-24. DOI:
581 10.1017/S0022112096004594
- 582 Sciacchitano, A., Wieneke, B., 2016. PIV uncertainty propagation. *Meas. Sci. Technol.* 27,
583 084006. DOI: 10.1088/0957-0233/27/8/084006.

- 584 Taylor, Z. J., Gurka, R., Kopp, G. A., 2014. Effects of leading edge geometry on the vortex
585 shedding frequency of an elongated bluff body at high Reynolds numbers. *J. Wind Eng.*
586 *Ind. Aerodyn.* 128, 66–75. DOI: 10.1016/j.jweia.2014.03.007
- 587 Turbulent Flow Instrumentation (TFI), 2017.
588 <https://www.turbulentflow.com.au/Products/CobraProbe/CobraProbe.php> (Last date of
589 access: Sep. 1, 2017)
- 590 van Oudheusden, B. W., Scarano, F., Roosenboom, E. W. M., Casimiri, E. W. F., Souverein, L.
591 J., 2007. Evaluation of integral forces and pressure fields from planar velocimetry data for
592 incompressible and compressible flow. *Exp. Fluids.* 43, 153-162. DOI: 10.1007/s00348-
593 007-0261-y
- 594 van Oudheusden, B. W., 2013. PIV-based pressure measurement. *Meas. Sci. Technol.* 24,
595 032001. DOI: 10.1088/0957-0233/24/3/032001
- 596 Wilcox, D. C., 2007. *Basic Fluid Mechanics*, Third edition. DCW Industries, Inc., USA.
- 597

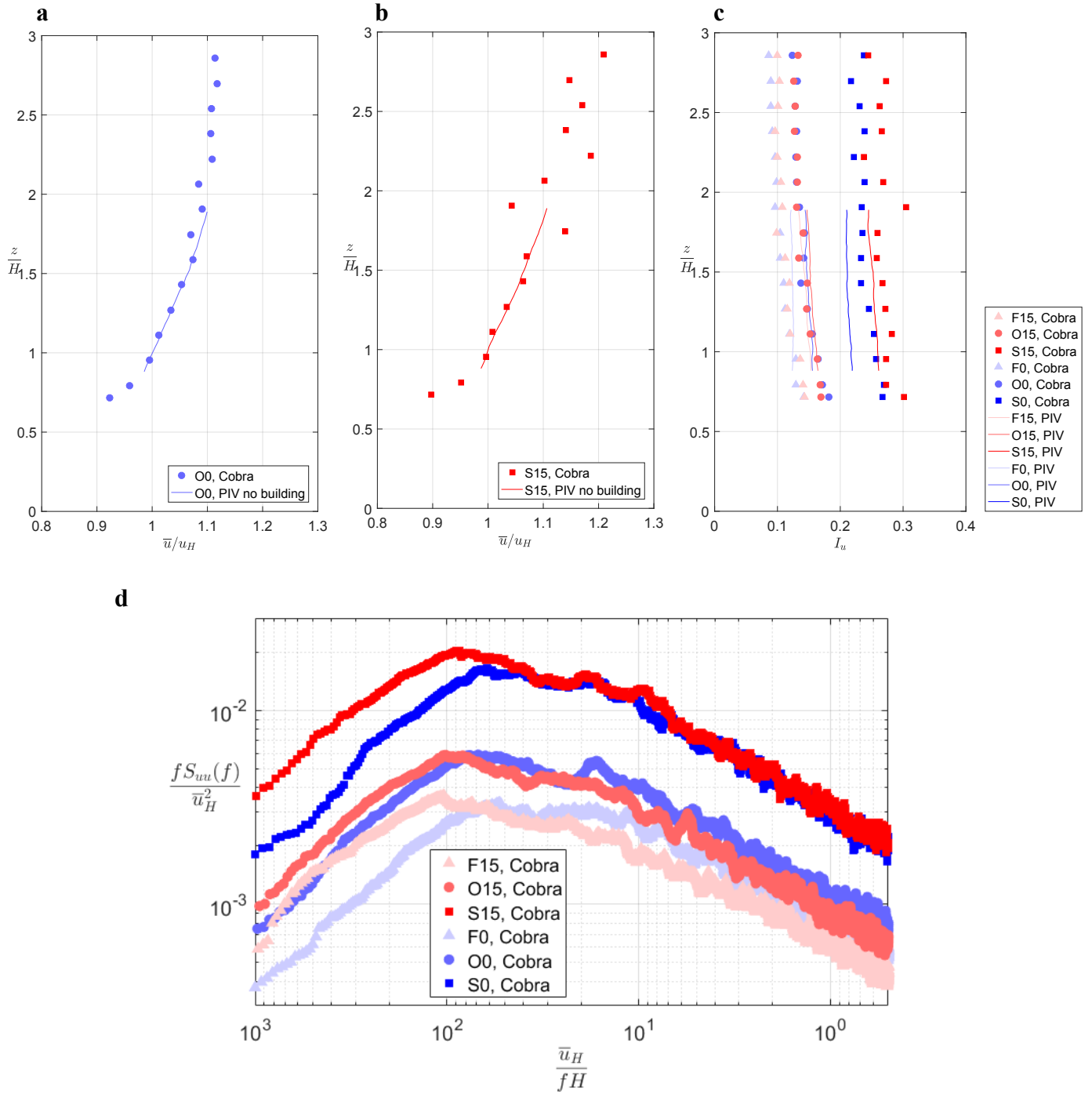


Figure 1: Mean streamwise, u , velocity for terrain (a) O0, and (b) S15 as measured by the Cobra probe and PIV, and (c) turbulence intensity profiles measured with the Cobra probe, along with (d) reduced spectral density of the streamwise velocity at roof height for the 6 terrains.

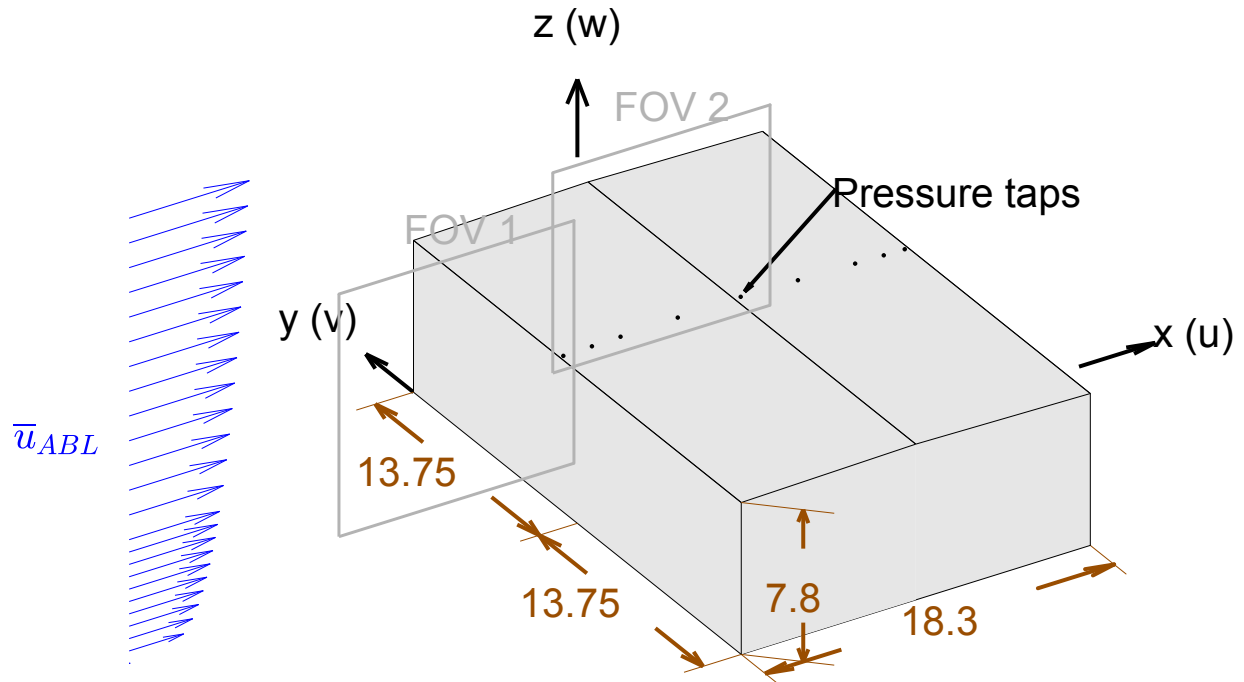


Figure 2: The low-rise building model along with planar fields of view (FOV) from the PIV measurements. The dimensions of the building model are labelled with units in centimeters. FOV-1 has a plane dimension of $\Delta x \times \Delta z = 12.3 \text{ cm} \times 12.4 \text{ cm}$, with the bottom boundary and right boundaries aligned with $z = 3.14 \text{ cm}$ and $x = -0.18 \text{ cm}$, respectively. FOV-2 has a plane dimension of $\Delta x \times \Delta z = 11.4 \text{ cm} \times 10.3 \text{ cm}$, with the bottom boundary and left boundaries aligned with $z = 8.11 \text{ cm}$ and $x = -1.29 \text{ cm}$, respectively.

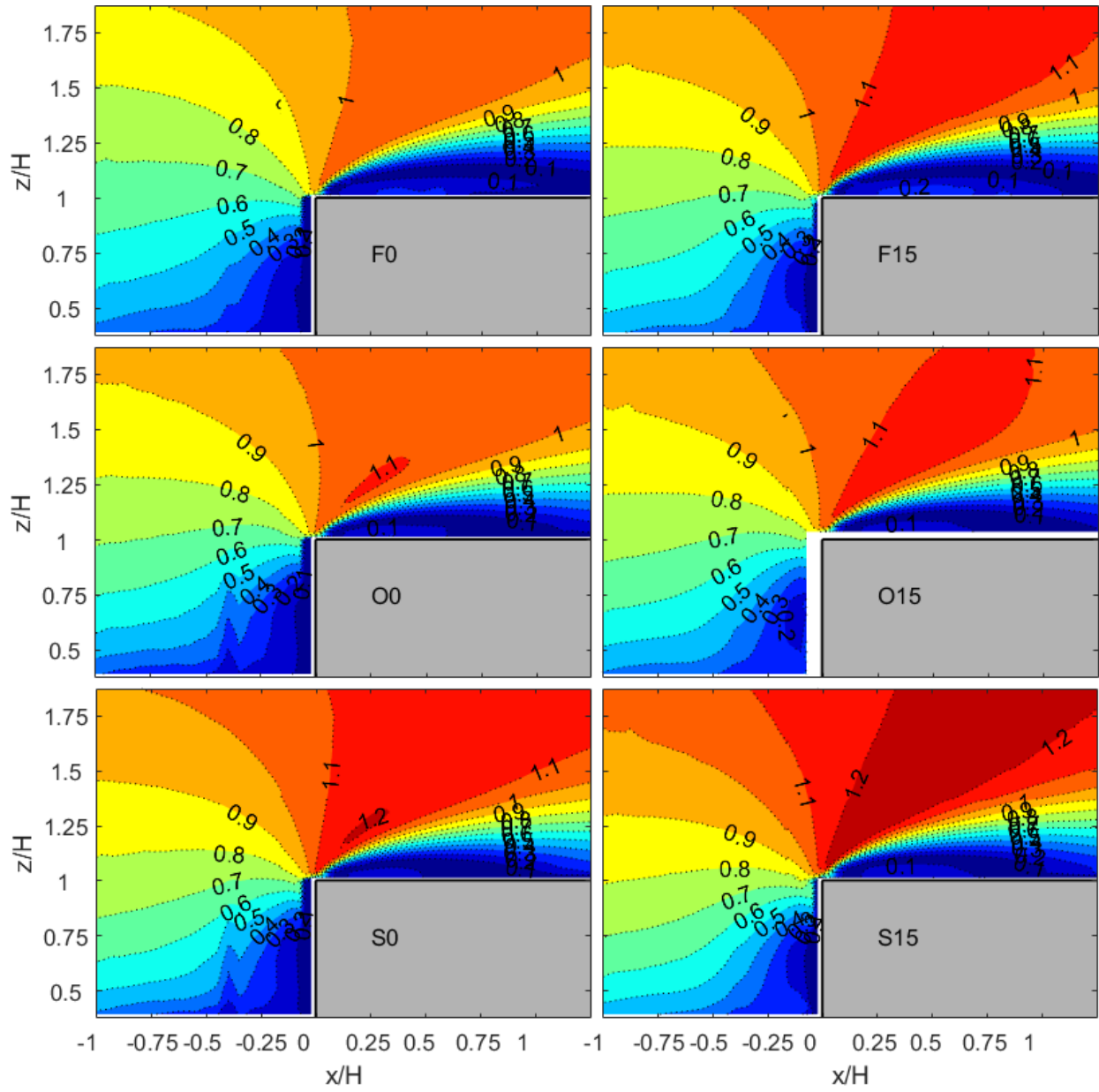


Figure 3: Mean velocity ratio, $|\bar{\mathbf{u}}|/u_{ref}$, near the roof obtained for the six terrains.

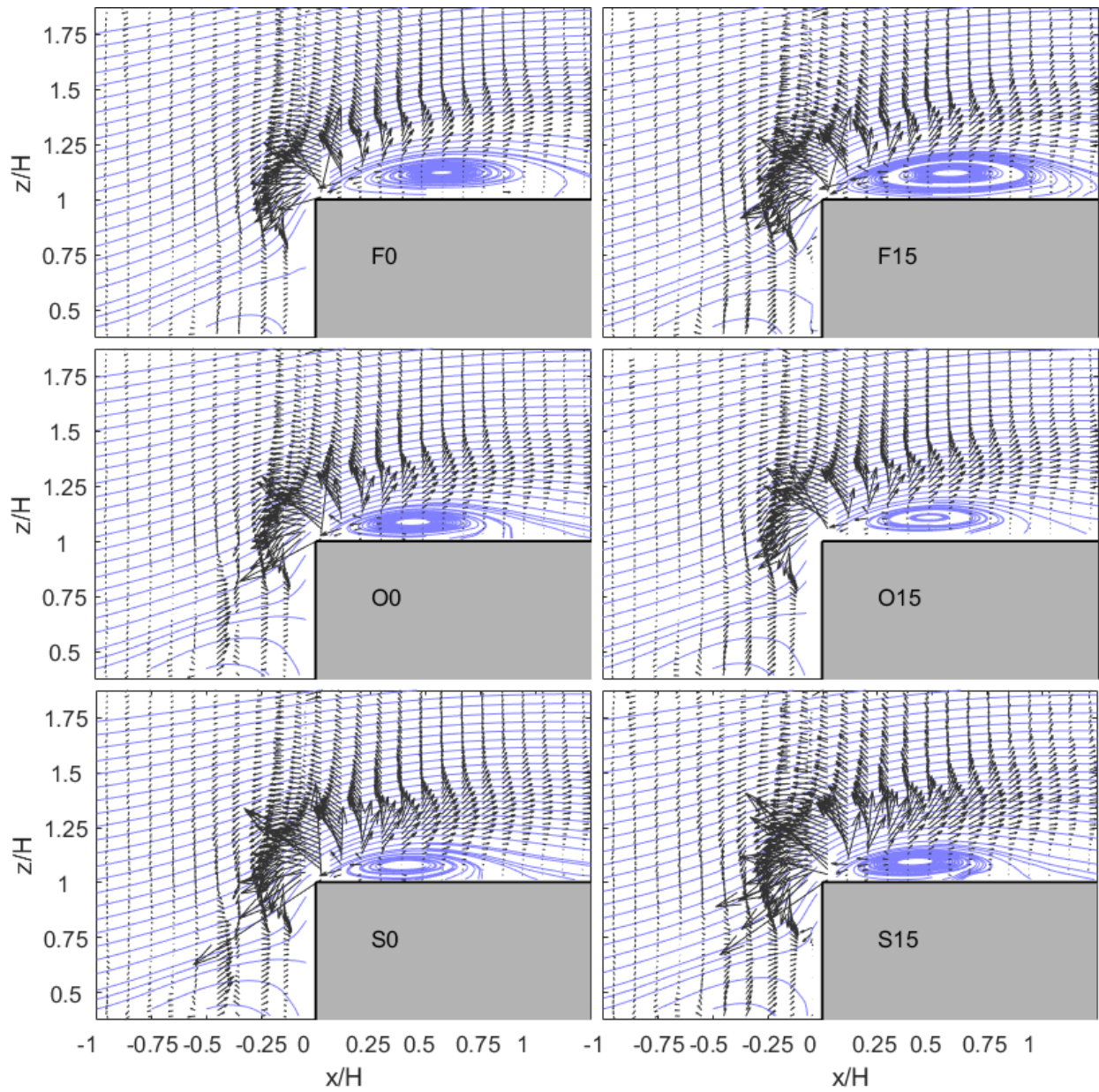


Figure 4: Pressure gradient vectors for the mean convection term in the Navier-Stokes equations for the six terrains, along with streamlines. (Note that only one of every four vectors is shown in the x-direction.)

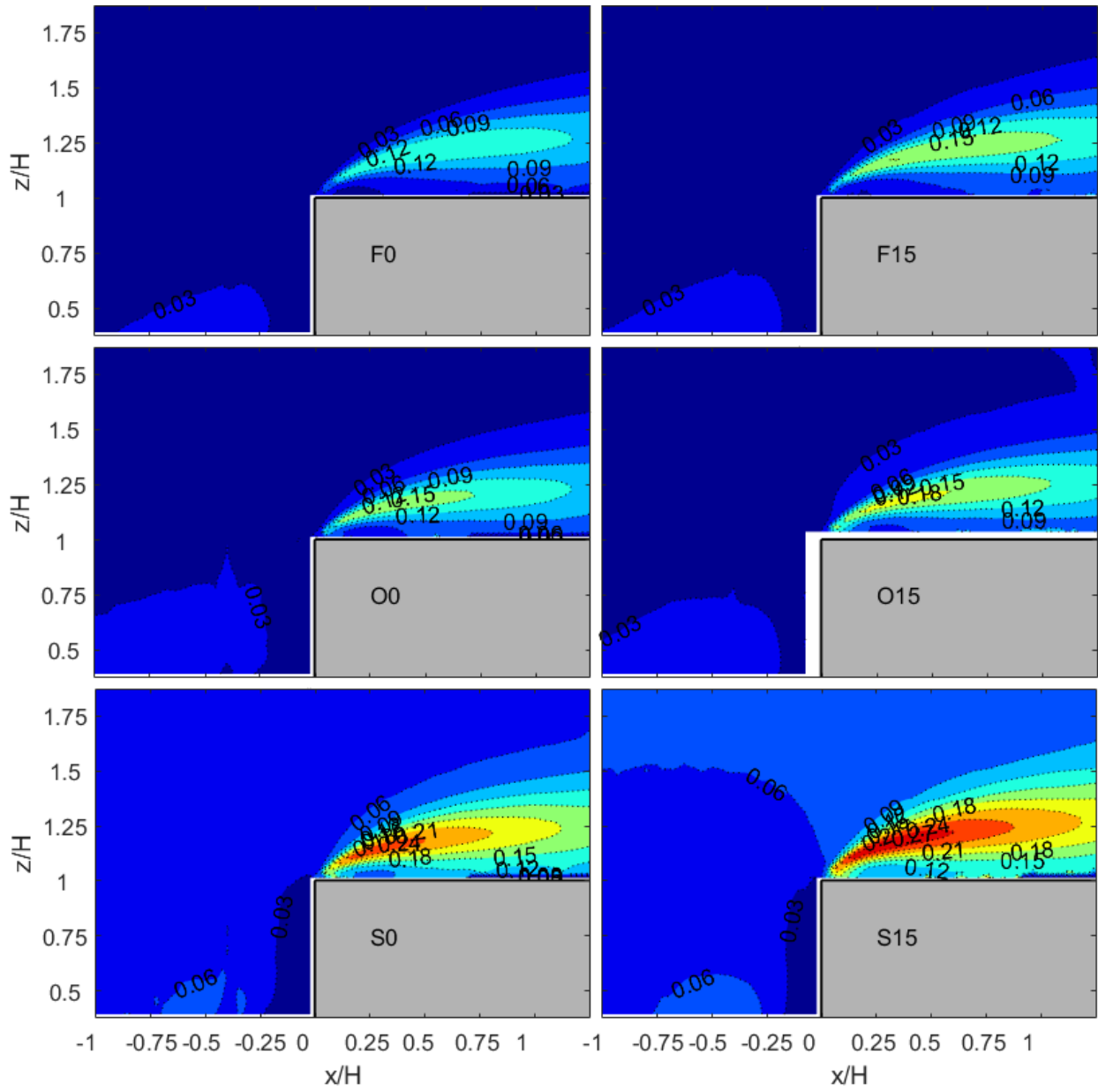


Figure 5: Streamwise Reynolds normal stresses, $\overline{u'u'}/u_{ref}^2$, for the six terrains.

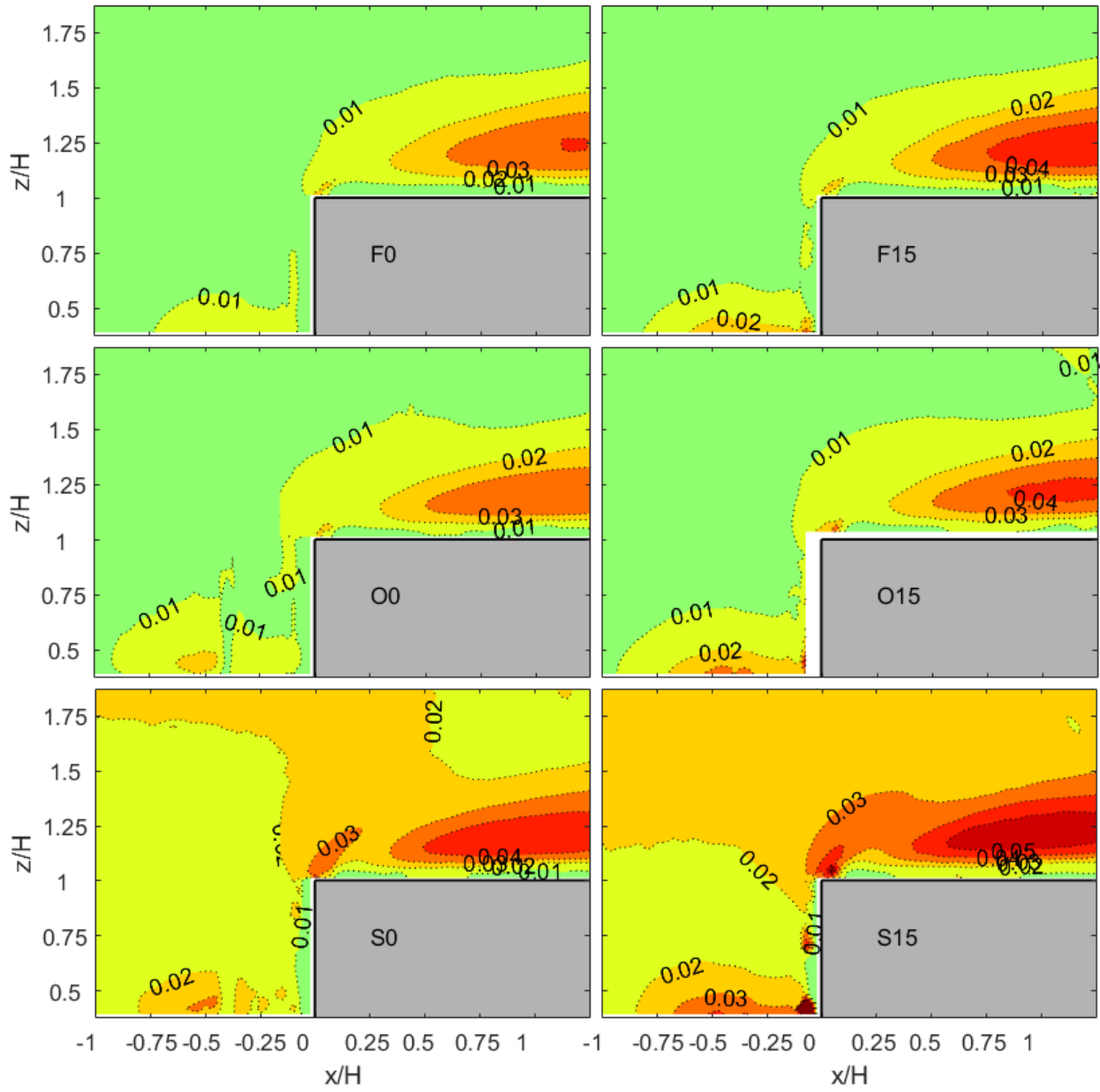


Figure 6: Vertical Reynolds normal stresses, $\overline{w'w'}/u_{ref}^2$, for the six terrains.

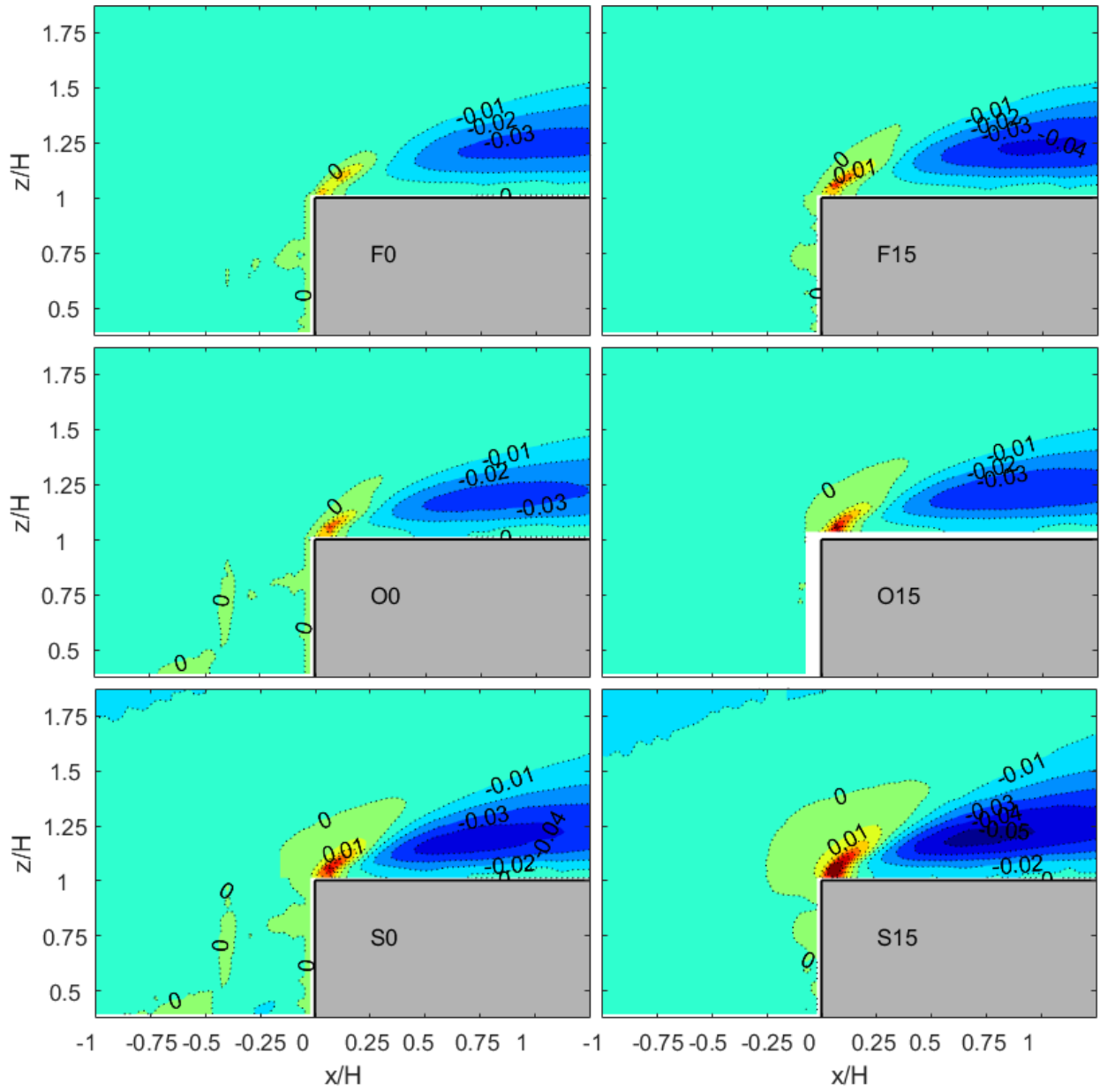


Figure 7: Reynolds shear stresses, $\overline{u'w'}/u_{ref}^2$, for the six terrains.

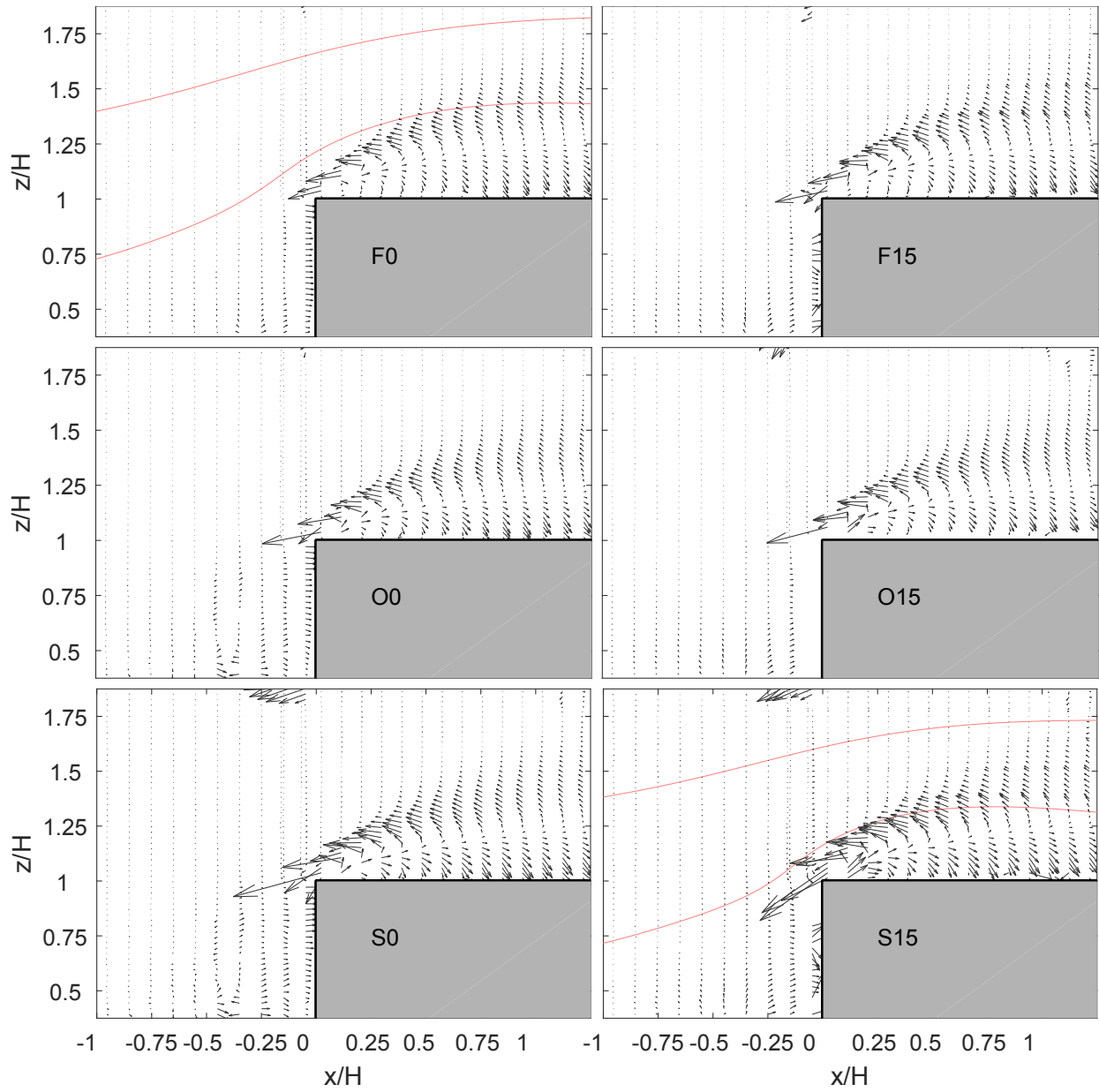


Figure 8: Pressure gradient vectors for the turbulence term in the Navier-Stokes equations for the six terrains. (Note that only one of every four vectors is shown in the x-direction.)

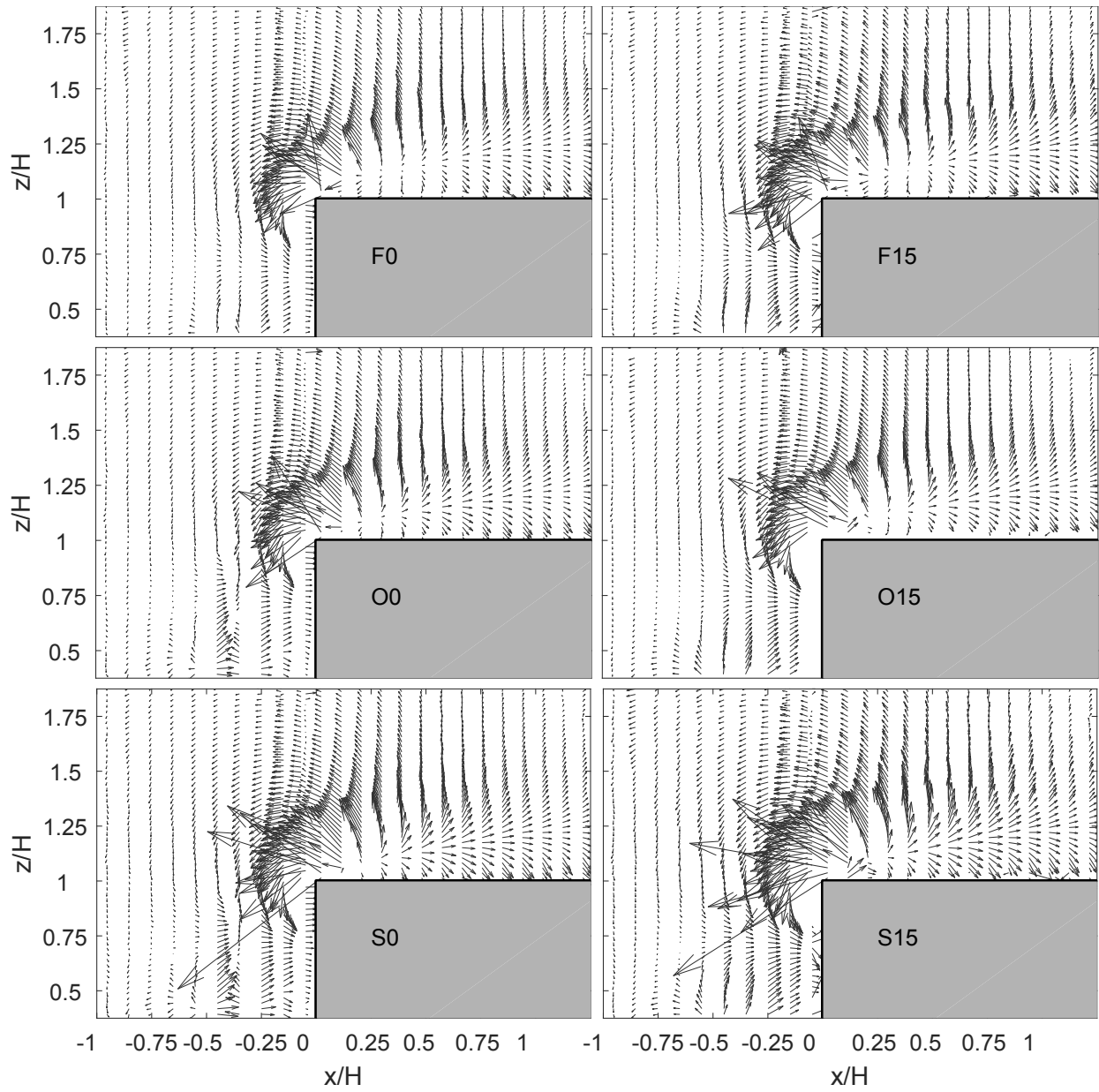
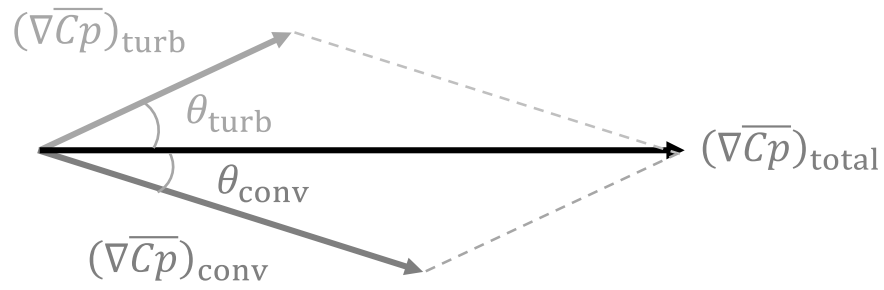
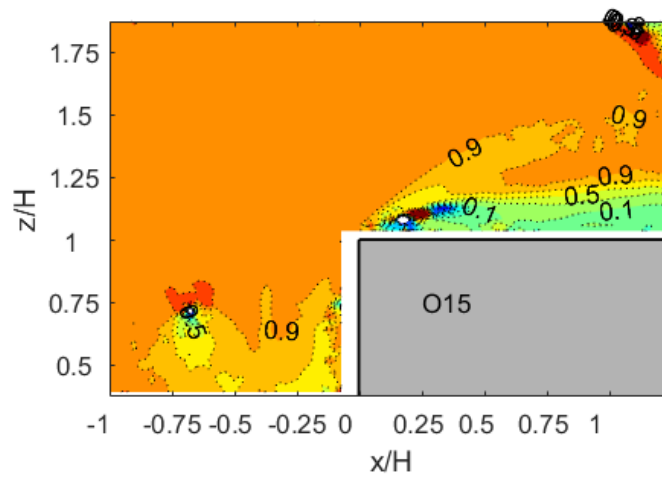


Figure 9: The total pressure gradient vectors for the six terrains. (Note that only one of every four vectors is shown in the x-direction.)

a



b



c

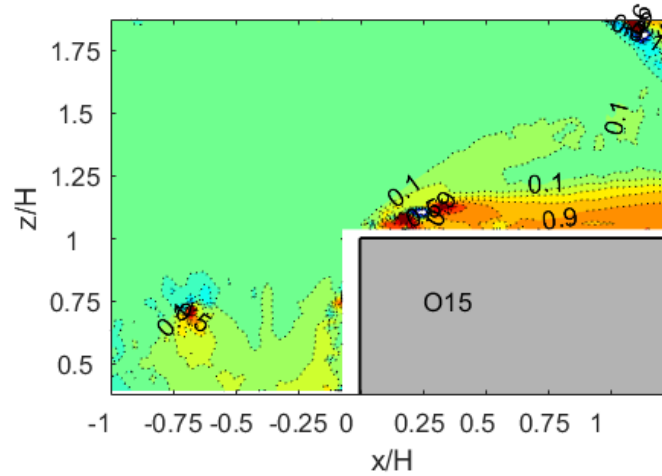


Figure 10: (a) Schematic of total pressure gradient vector at a point, along with the contours of the contributions of the (b) convection and (c) turbulence terms for the terrain, O15.

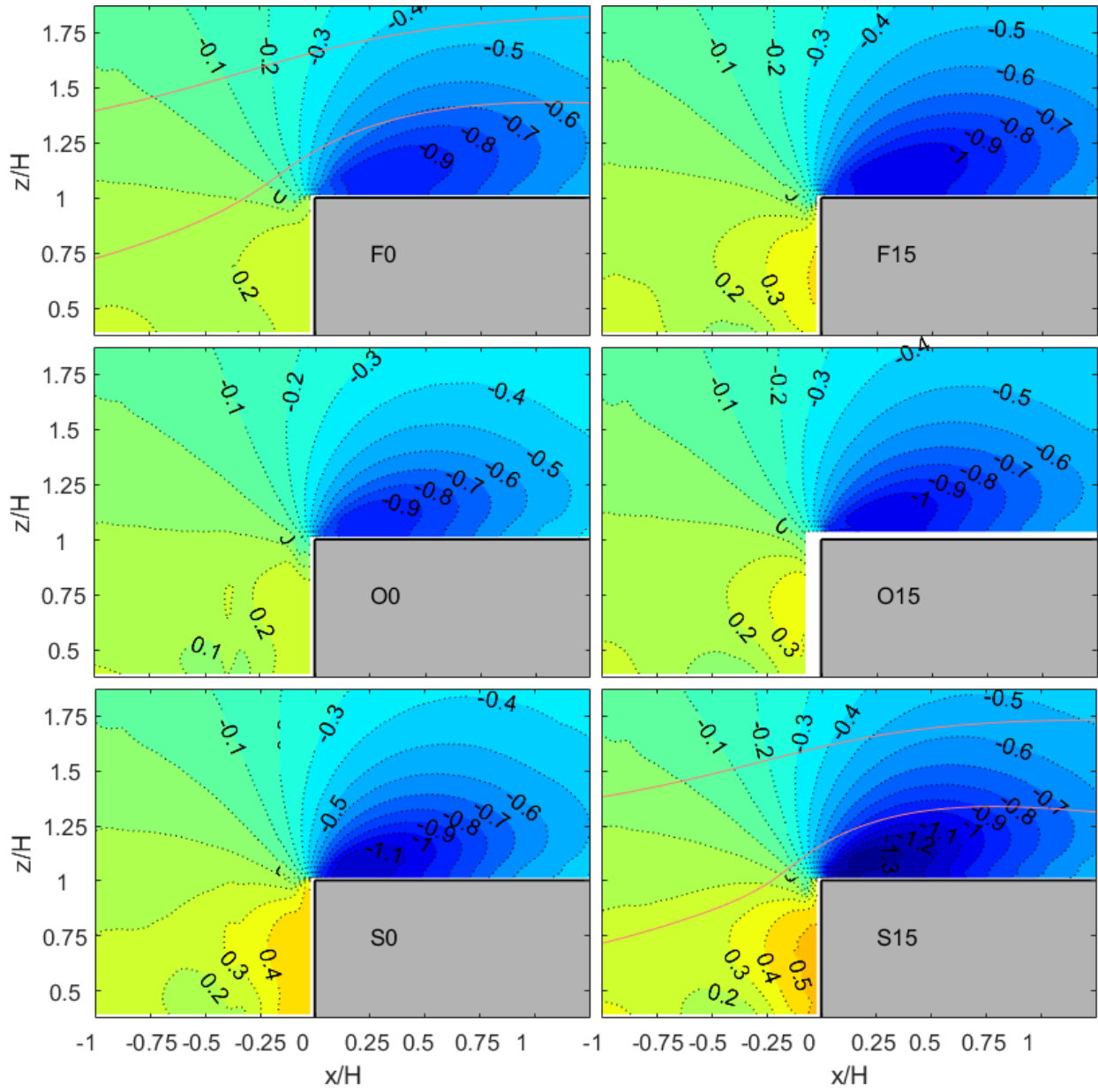


Figure 11: The mean pressure, $\overline{C_p}$, fields obtained using the analytical interpolation technique for the six terrains.

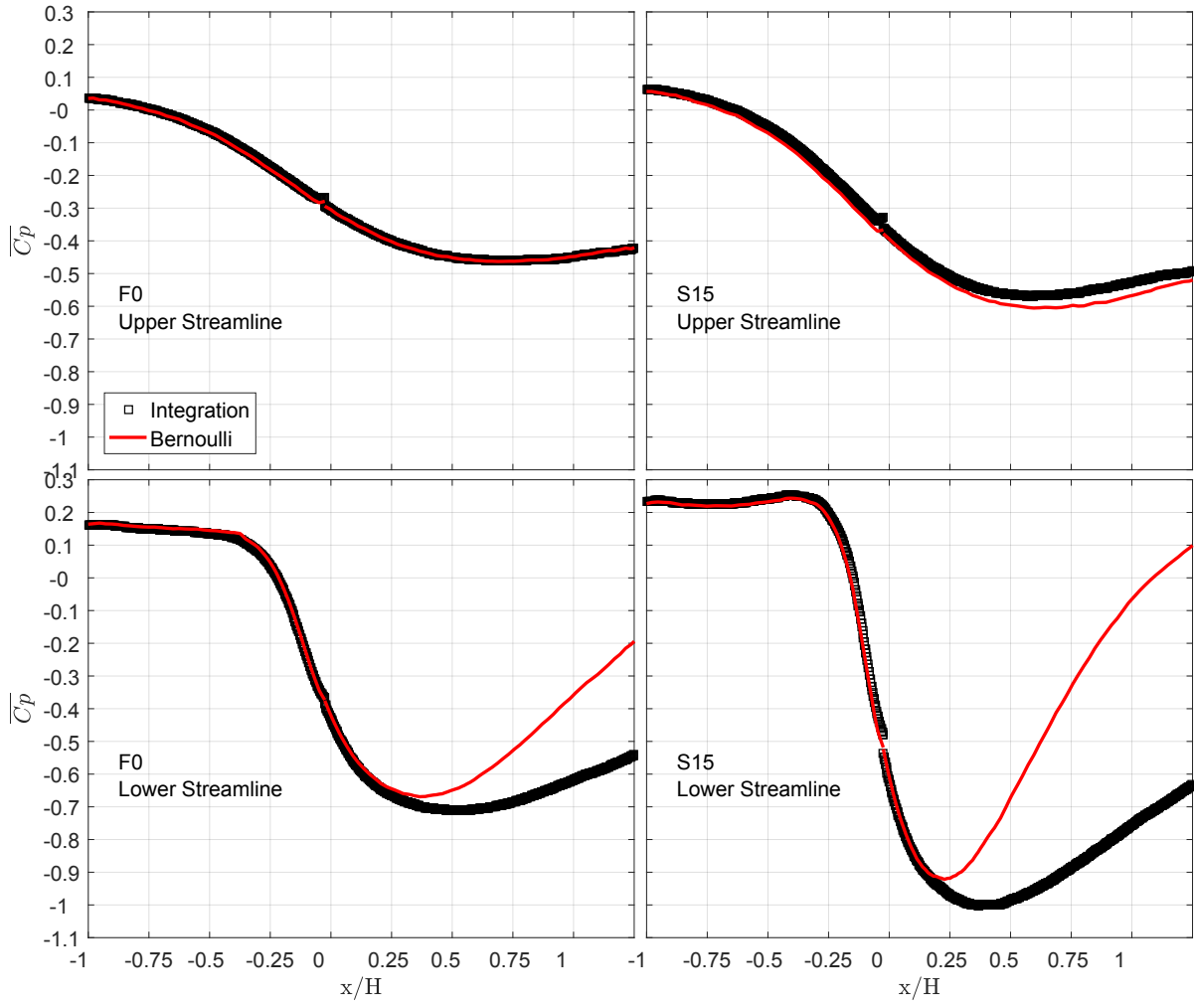


Figure 12: The mean pressure, $\overline{C_p}$, obtained from the analytical interpolation technique and from Bernoulli's equation along upper and lower streamlines in terrains 'F0' and 'S15'.

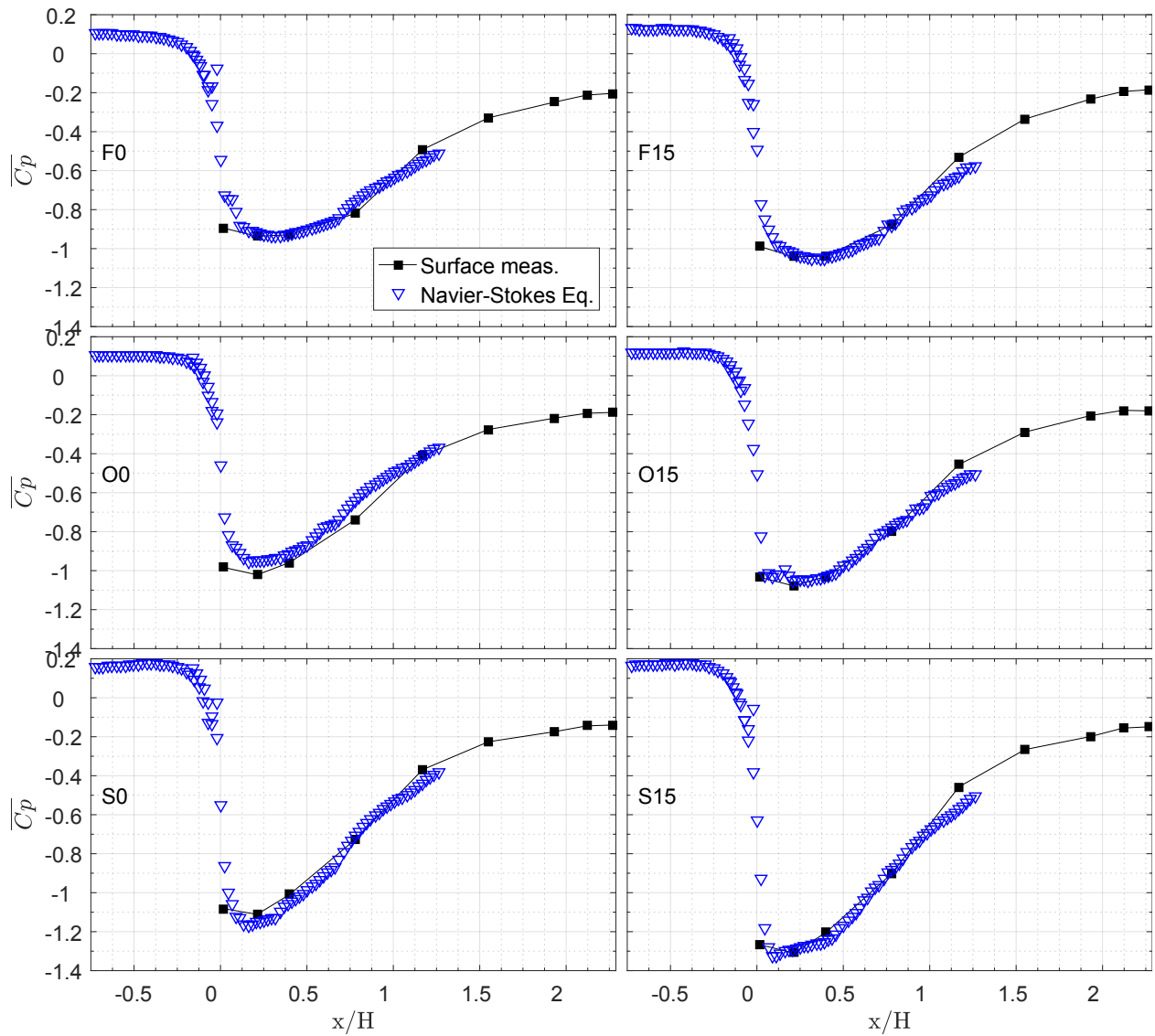


Figure 13: Mean pressure coefficients on the roof surface, $\overline{C_p}$, obtained from measurements and the analytical interpolation technique for the six terrains.

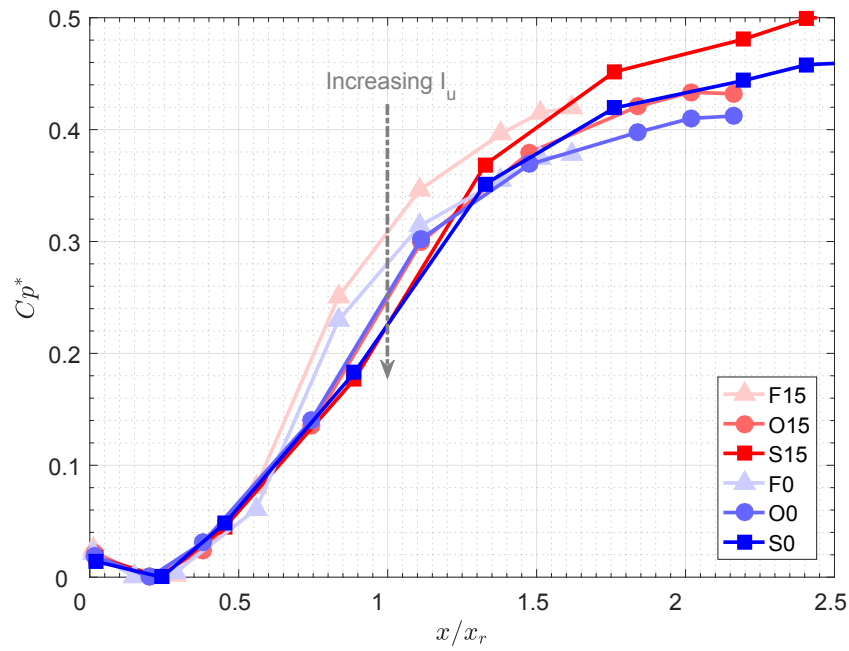


Figure 14: Reduced pressure coefficient C_p^* obtained from surface pressure measurements for the six terrains (Akon and Kopp, 2016).